



Experimental nonlinear dynamic regimes for energy harvesting from cantilever bistable shells[☆]

Andrzej Mitura^a, Matteo Brunetti^b, Lukasz Kloda^{a,*}, Francesco Romeo^c, Jerzy Warminski^a

^a Department of Applied Mechanics, Lublin University of Technology, Nadbystrzycka 36, Lublin, 20-618, Poland

^b Polytechnic Department of Engineering and Architecture, University of Udine, via delle Scienze 206, Udine, 33100, Italy

^c Department of Structural and Geotechnical Engineering, University of Roma La Sapienza, via Eudossiana 18, Rome, 00184, Italy

ARTICLE INFO

Communicated by D. Yurchenko

Keywords:

Bistable shells
Energy harvesting
Snap-through effect
Experimental testing
Piezoelectric patches

ABSTRACT

An experimental campaign on a cantilever composite bistable shell with a piezoelectric patch is reported in the paper. The considered shell is characterized by two stable configurations far apart in terms of natural frequencies and geometries. Harmonic forcing is applied at the shell's clamped side through an electrodynamic shaker and the dynamic response is measured through an embedded strain gauge. Different dynamic regimes are encountered by performing excitation frequency and amplitude sweeps. The resonance scenarios around the two natural frequencies corresponding to the stable configurations show different softening behavior. The excitation amplitude threshold level for snap-through motion is identified. Experimental power generation maps plotted on the excitation frequency–amplitude plane are created to provide useful design insights for vibration energy harvesting purposes.

1. Introduction

The mechanical properties exhibited by bistable shells have raised considerable research interests over more than three decades. Two stable equilibrium positions easily attainable by composite structures with large deformations and little energy have found numerous engineering applications. Aerospace, bionics, passive vibration isolation, energy harvesting are the main fields of application so far explored. Examples of recent significant applications are: aircraft morphing wings [1]; shape morphing microrobot in medicine [2]; shape morphing structure in civil engineering [3]. By dynamically activating the transition between the equilibrium positions a variety of dynamic regimes of the bistable composite shells can be triggered enabling advantageous operating conditions.

The bistability can be obtained in several ways, e.g. by initial load/deformation causing the buckling and leading to two stable equilibria [4], by use of magnets, which attract or repel the structure to new stable equilibria [5], etc. The latter mentioned examples of bistability can be of little importance in real applications, because of the need for additional elements (e.g. magnets) which will prevent their use (e.g. aircraft wing). Therefore, among the available different sources of mechanical bistability the one associated to the curing residual stresses in unsymmetric composite laminates has been the most extensively exploited. Comprehensive literature reviews on bistable composite laminates can be found in Emam and Inman [6], Zhang et al. [7].

For unsymmetric composites, square shells with external excitation applied at the center of the laminate and free boundary conditions were mostly considered so far. The initial studies gave mostly experimental evidence of the so called in-well and cross-well dynamic regimes [8–10]. Afterwards, several modeling strategies have been proposed to interpret and predict their nonlinear

[☆] The work is financially supported by grant 2021/41/B/ST8/03190 from the National Science Centre, Poland.

* Corresponding author.

E-mail address: l.kloda@pollub.pl (L. Kloda).

<https://doi.org/10.1016/j.ymssp.2023.110890>

Received 3 July 2023; Received in revised form 13 September 2023; Accepted 23 October 2023

Available online 10 November 2023

0888-3270/© 2023 The Authors.

Published by Elsevier Ltd.

This is an open access article under the CC BY license

(<http://creativecommons.org/licenses/by/4.0/>).

dynamic behavior [11–14]. Time-varying principal curvature have been proposed in Zhang et al. [15] to directly describe dynamic snap-through phenomena. The unsymmetric square composite laminate was also considered in Wu et al. [16] where experimental and numerical bifurcation diagrams, phase portraits, power spectra, and Poincaré maps were presented to illustrate periodic and chaotic dynamic regimes. A further interesting dynamic regime, the so-called metastable chaos, was theoretically obtained in Liu et al. [17] by introducing a large enough parametric excitation able to give birth to three wells in the potential function.

Aiming to maximize the kinetic energy associated to snap-through motion, further geometric configurations and boundary conditions were considered. Four-corner simply supported bistable unsymmetric composite shell was recently considered in Wu et al. [18]. In this work analytical and numerical studies are presented to show the influence of the initial curvature radius on the critical load governing the onset of snap-through regime. The influence of amplitude and frequency of the excitation was discussed in Guo et al. [19] including experimental results.

Cantilevered boundary conditions were also considered by several researchers. The nonlinear dynamics of a bistable laminate with two remarkably different stable geometric configurations was considered by the authors in Brunetti et al. [20]. The considered bistable composite shells are obtained by inducing a prestress on initially curved stress-free configurations [21–24]. Therefore, the asymmetry of the clamped stable states is controlled by the curvature of the shell's stress-free configuration. It is shown that the relevant difference between the shell's stable shapes triggers a level of kinetic energy extracted usually not achievable with the symmetric stable shapes.

More recently, a laminated cantilever shell modeled as a two-degree-of-freedom nonlinear dynamic system based on the curvature-displacement relationships was studied in Ren et al. [25]. Analytical and FEM results are presented to discuss the effect of the variations of frequency and amplitude of the external excitation on the dynamic snap-through and nonlinear vibrations' scenarios.

The rich nonlinear dynamic response which entails large amplitude vibrations with relatively small excitation energy is prone to be exploited for energy harvesting applications.

Among the initial experimental studies on a square bistable plate with piezoelectric patches, in Arrieta et al. [26], it was shown that large average power can be harvested from nonlinear oscillations. Square composite shells were also considered in Betts et al. [27], Betts et al. [28], Betts et al. [29]. In these works, the sensitivity of the harvesting performance with respect to the bistable system design parameters was investigated; repeatable snap-through motion was shown to allow the most effective power generation. Unsymmetric cross-ply square laminates with piezoelectric patches were also considered in Jiang et al. [30] by means of a three-degree-of-freedom nonlinear electromechanical system. The obtained numerical results give qualitative evidence of the harvesting performance for different excitation amplitude levels and different dynamic regimes confirming that the highest power generation is obtained during dynamic snap-through.

The energy harvesting advantages of a bistable asymmetric laminates coupled to piezoelectric materials was also studied for a cantilevered configuration in Harris et al. [31]. In Taki et al. [32], Lee and Inman [33] analytical models were proposed to describe square laminates with piezoelectric layers. In the latter the model enabled to produce accurate voltage and power outputs of a piezoelectric bistable laminate under nonlinear cross-well vibrations. In a recent review paper [34] an overview of the ongoing research on bistable composites for energy harvesting applications is provided.

Despite the conspicuous literature on the nonlinear dynamics of bistable shells and its impact on the potential for energy harvesting the results are limited mainly to the structures with two stable configurations which differ slightly. Furthermore, a thorough experimental analysis of composite cantilever shells with piezoelectric patches still seems to be lacking. In [20] the dynamics of shells with significantly different stable equilibria shapes was investigated, highlighting some difficulties in triggering reversible snap-through effects. The main goal of this paper is to experimentally explore reversible snap-through effects in the dynamic response of a real composite shell. Such response includes the effects of unavoidable manufacturing imperfections as well as MFC patch interactions, both difficult to be modeled. The study also aims to identify all possible types of motion and to select which of them is the most effective for vibration energy harvesting. Towards these goals, a new shell design in terms of thickness, material properties and aspect ratio, is adopted. Moreover, in addition to standard analysis methods (such as resonance characteristics, Fast Fourier Transform, Poincaré maps), new procedures for dynamic regime detection and classification are proposed, including a novel energy recovery index.

The paper is organized as follows. In Section 2 the bistable shell manufacturing details are reported highlighting its geometric and mechanical properties. Next, in Section 3, the experimental campaign under harmonic forcing applied at the shell's clamped side through an electrodynamic shaker is presented; it focuses on the shell's strain response at resonance, around the stable configurations, and during snap-through motion.

In Section 4, the energy harvesting performance corresponding to the different dynamic regimes encountered in the experimental analysis is discussed. Power generation maps on the excitation frequency–amplitude plane are created to provide useful direct design indications. Concluding remarks and future developments are reported in the last Section.

2. Cantilever bistable shell manufacturing

This work extends the investigations presented in two previous works by Brunetti et al. [22], Brunetti et al. [20]. In Brunetti et al. [22] the possibility of realizing clamped multistable shells having significantly different stable equilibrium configurations was experimentally demonstrated. Starting from a composite shell with rectangular planform and pseudo-conical stress free shape, a cantilevered multistable shell was obtained by flattening and clamping one of its short edges. An 8-layer angle-ply anti-symmetric stacking sequence $[45/-45_2/45/-45/45_2/-45]$ was used, with an Hexcel's "Hex Ply" carbon-epoxy composite prepreg as

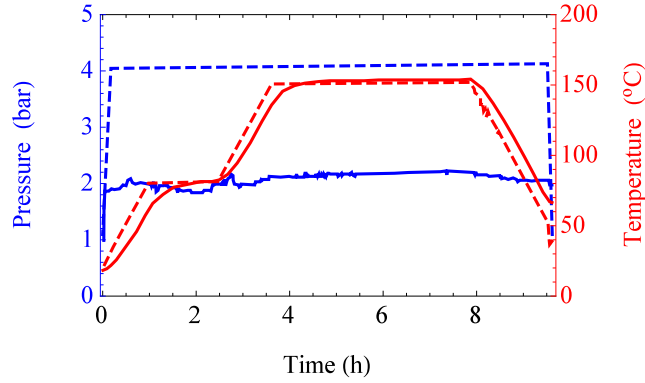


Fig. 1. The autoclave control process of the shell curing in time domain: temperature of bag thermocouple/chamber air — red solid/dashed curves, pressure in the bag/chamber — blue solid/dashed curves. (For interpretation of the references to color in this figure legend, the reader is referred to the web version of this article.)

Table 1
Mechanical properties of carbon-epoxy composite tested as recommended in [35].

E_1	E_2	G_{12}	ν_{21}	ν_{12}	ρ	t_ℓ
GPa	GPa	GPa	–	–	kg/m ³	mm
120.58	9.67	13.19	0.32	0.02	1532 ± 2	0.038

an elementary layer. Two prototypes were created: the first was of pseudo-cylindrical shape, with curvatures of the free and clamped edges of the same sign; the second had the same curvatures of opposite sign. As predicted by theoretical model, once clamped, both prototypes exhibited multiple stable equilibrium configurations. Depending on the sign of curvature, a different number of stable equilibria was found. Two equilibria were detected for the same signs of pseudo radii while for the shell with opposite signs four stable equilibria were observed [22]. In Brunetti et al. [20] an initial experimental and numerical study on the dynamics of this class of shells (that is, a relevant shape difference between the stable equilibrium configurations) was reported. The large amplitude nonlinear dynamic behavior of the pseudo-cylindrical shell prototype was studied via a reduced 1DoF nonlinear oscillator with double potential well. This latter was used to extend the dynamic analysis to ranges of amplitudes and frequencies of excitation wider than the experimentally attainable ones. For the tested shell prototype the two-well domain of oscillations was too narrow to be of practical interest for energy harvesting purposes; moreover, the transition from one stable configuration to the other turned out to be not reversible.

On the basis of the mentioned previous studies, an ad-hoc design of the shell structural parameters is presented in this work aiming at both widening the domains of two-well oscillations and realizing a reversible transition. The new design was guided by the information gathered from the 1DoF nonlinear oscillator. In particular, to facilitate a reversible shell's transition between the two stable configurations, it was decided to decrease both the aspect ratio and the stiffness.

2.1. Shell description: mechanical and geometric properties

The thin-walled pseudo-conical shell is made of carbon-epoxy composite prepreg tape (*AS4-GP-12K_40gsm-300 mm-ThinPregI35EP*). Prior to the curing process, the composite single layer is characterized by unidirectional reinforcement and thickness 0.04 mm. The manufacturing standard samples for strength tests in the autoclave process reduces to about $t_\ell = 0.038$ mm, the average thickness of one layer of the flat sample with a 5 % material shrinkage across the thickness. The autoclave process is strongly related to the thermal and chemical shrinkage effect, which influences zones of multi-stability and affects the dynamic behavior of the structure. An incorrectly performed curing process can cause e.g. loss of multi-stability or significantly change the potential wells. Fig. 1 presents characteristics of the manufacturing process which should be maintained to guarantee reproducibility of the production and the dynamics properties of the shell prototype. Properties of the unidirectional strength test specimens are gathered in Table 1.

In this study a new shell is manufactured on the same mold adopted in Brunetti et al. [20]. The mold's top reference surface is described by the function (see Fig. 2)

$$w_0(x_1, x_2) = \left[\frac{1}{r_0} + \left(\frac{1}{r_f} - \frac{1}{r_0} \right) \frac{x_1}{L_1} \right] \frac{x_2^2}{2} + \Delta w, \quad (1)$$

where $\Delta w = 0.0005$ m specifies the offset from the mid-surface and takes into account half of the shell's thickness plus peel ply. L_1 defines a distance between planes x_2x_3 and ϕ_3 on which construction curves are projected. Constants $r_0 = 0.114$ m and $r_f = 0.07$ m describe pseudo radii of the conical shape at $x_1 = 0$ and $x_1 = L_1$, respectively. $L_1 = 0.45$ m affects the transition

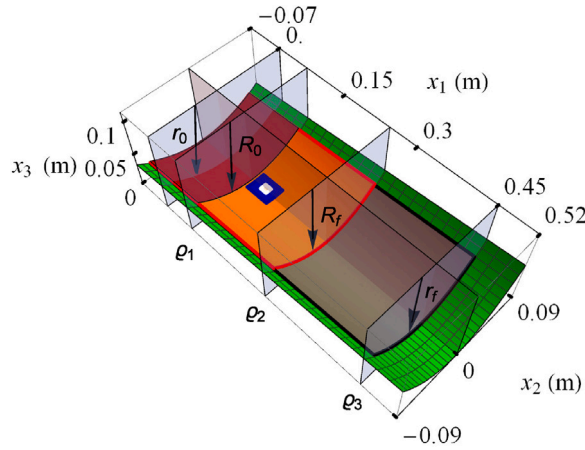


Fig. 2. The function w_0 describes the top surface of the mold (green checkered), the shell dimensions with the ratio of 3: 1 with a clamping margin studied in Brunetti et al. [22] (gray) and the dimensions of the shell under investigation — gripping (red) and cantilever (orange) parts. The MFC patch $M2814 - P1$ (blue) and strain gauge 120Ω (white) are embedded on concave and convex sides of the shell, respectively. (For interpretation of the references to color in this figure legend, the reader is referred to the web version of this article.)

of the shape between the curvatures (r_0 and r_f), and at the same time defines the angle of inclination of the shell along x_1 -axis for $x_2 \neq 0$ m. The shell is situated within the range of $-0.075 \text{ m} < x_2 < 0.075 \text{ m}$, resulting in a width dimension of $L_2 = 0.15 \text{ m}$, which remains consistent with the previous analyses. Fig. 2 shows the top surface of the mold. The original aspect ratio of the shell, made of M12/35%/UD134/AS7/300 lamina, was 3:1. The tested specimen is obtained by trimming the original shell and equipping it with harvesting and sensing devices. The working length of the shell has been trimmed at $x_1 = 0.245 \text{ m}$. The coordinate $-0.105 \text{ m} \leq x_1 \leq 0.065 \text{ m}$ maintains shape continuity according to function $w_0(x_1, x_2)$ in Eq. (1), and defines the clamping depth. Therefore, the active length of the composite shell ranges from $x_1 = 0.065 \text{ m}$ to $x_1 = 0.245 \text{ m}$, and in the unclamped (rest) configuration corresponds to about 0.18 m cantilever length. The pseudo radii of the proposed shell are projected on two limit planes ϕ_1 and ϕ_2 , and take the values $R_0 \approx 0.1045 \text{ m}$ and $R_f \approx 0.08493 \text{ m}$.

It is easy to see that the surface contains a bottom line at $x_2 = 0$ which intersects x_1 axis ($x_3 = 0 \text{ m}$) and has a smaller curvature in the gripping part than at the free end. Moreover the cone's angle inclination is given by

$$\frac{\partial w_0(x_1, x_2)}{\partial x_1} = \left(\frac{1}{r_f} - \frac{1}{r_0} \right) \frac{x_2^2}{2L_1} = 6.12643x_2^2. \quad (2)$$

It means that the slope angle is independent of the dimension x_1 (constant at given x_2).

Most of the experimental studies available in the wide literature focus on stacking the composite plate on a flat table, and the morphing effect comes from the shrinkage of the asymmetric material in the curing process. The pseudo-conical shells allow to design equilibrium states after practical clamping of one end, but the seemingly simple geometry of the mold poses a great challenge in the specimen production by autoclave technique. First, the prepreg tape is stacked in asymmetric sequence [45/−45₂/45/−45/45₂/−45] on a flat table. The stress-free uncured composite is aligned on mold's top surface, secured against movement during bagging, vacuuming and curing processes. The autoclaving parameters are presented in Fig. 1.

After manufacturing in autoclave process and cutting off the allowances to the length and width dimensions (see Eq. (1) and Fig. 2), the resulting shape is deviated by residual stresses arising due to resin chemical shrinkage. Thus, the crafted shell has been subjected to geometry measurements by GOM Atos 3D scanner, see Fig. 3a. Prior to vibration testing, the instrumentation (Figs. 3b and 3c) is attached to the shell as well — it is an additional factor that affects the specimen's geometry. High quality scan with saved 2 583 345 dots allows point cloud processing with 0.01 mm measurement accuracy. The results of the measures are presented in Fig. 4. The transparent film of the instrumentation prevents a correct scan, therefore, the thickness measurement is omitted in this area. The histogram presented in Fig. 4a indicates 92.39% of strips have height between 0.387 mm and 0.232 mm, on the other hand the most common thickness (38.58%) ranges from 0.31 mm to 0.271 mm. In forthcoming analyses the assumed thickness of single layer is consistent with Table 1, however we keep in mind that this is the average value of the composite formed as a plate in a unidirectional configuration. In the crafted shell the detected defects are the greater thickness for $y \leq 0$; and the diagonal connection strap of lamina tapes, which starts at the middle of the thinner edge and ends at the middle of the free end with larger curvature. In Fig. 4b the point cloud is superimposed using the best fit algorithm; the homogeneous distribution of the deviation analysis illustrates the shell twist effect in free (unclamped) configuration. We assume that it can be caused by many aspects e.g. the uncertainty of the human factor, the asymmetric sequence of layers, the curvature of the mold combined with the creeping and shrinkage of the epoxy resin in the curing process.

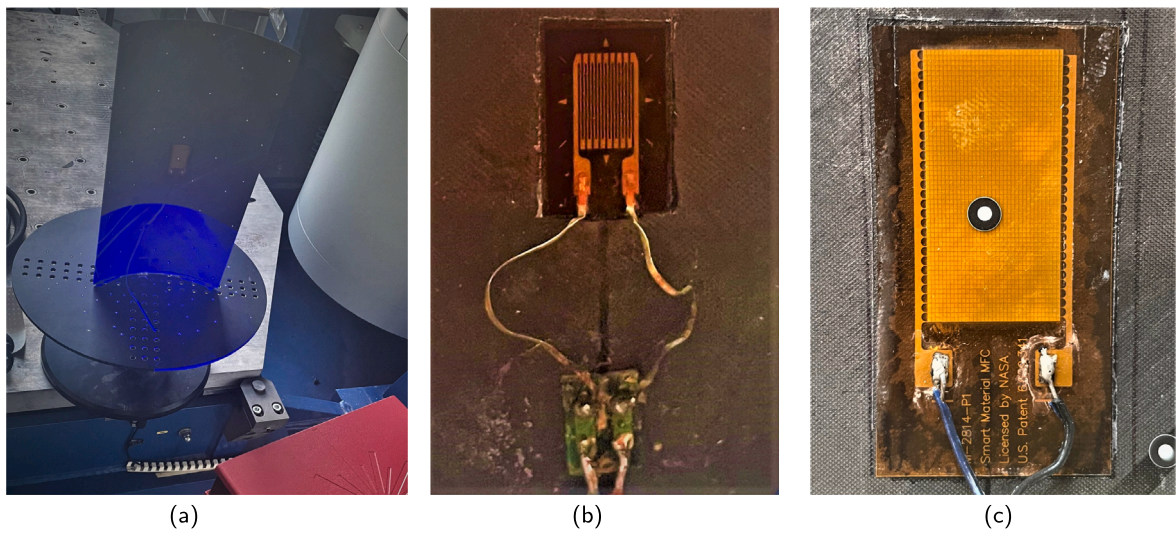


Fig. 3. (a) The shell with instrumentation on a turntable — scanning using the 3d scanner, (b) embedded strain gauge and (c) MFC patch. The vertical arrangement reduces the gravity effect during the table rotation and markers build reference measurement points.

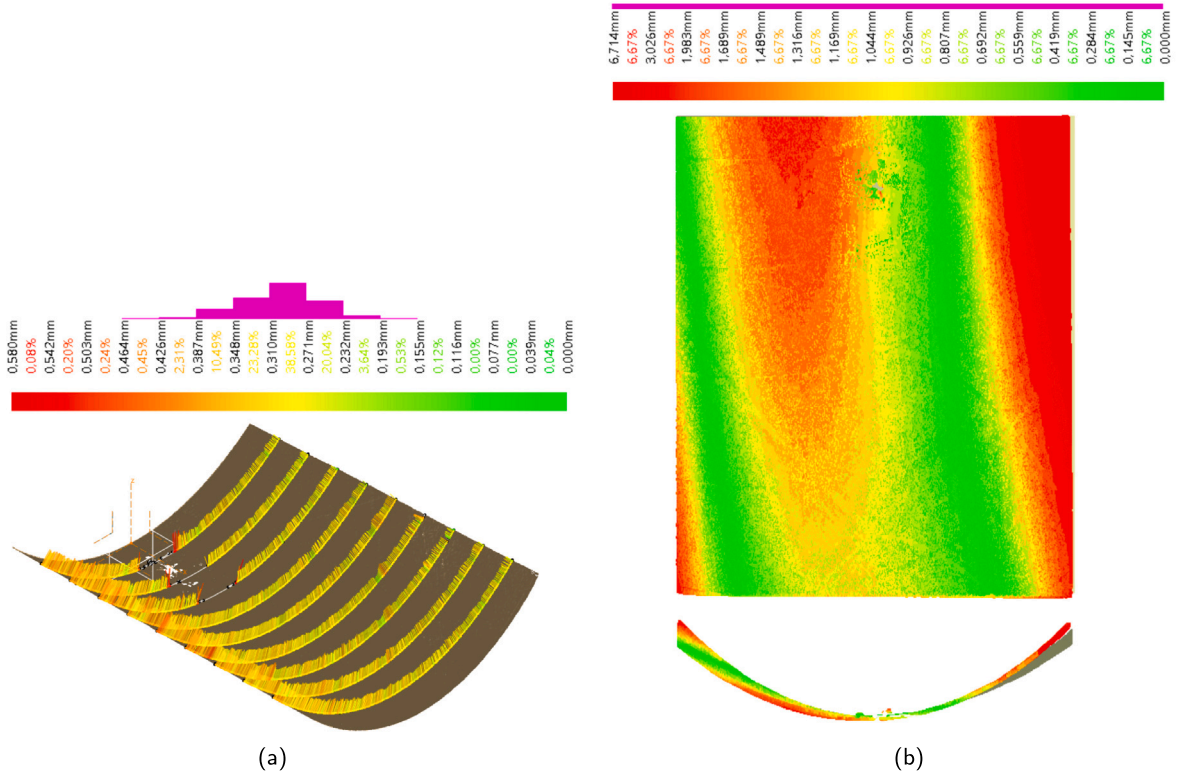


Fig. 4. (a) Thickness analysis of the operating part and (b) deviation analysis of the specimen with respect to reference shell (orange shell in Fig. 2 with $\Delta w = 0$) - top and front views. Top bars display histograms of considered domains, stripes demonstrate the thickness change at given sections and deviation maps highlight the effect of material shrinkage. (For interpretation of the references to color in this figure legend, the reader is referred to the web version of this article.)

2.2. Static bistability map

The bistability properties of the shell described in the previous subsection, after its $x_1 = 0.065$ m-edge is flattened and clamped, are analyzed using the reduced model presented in Brunetti et al. [21].

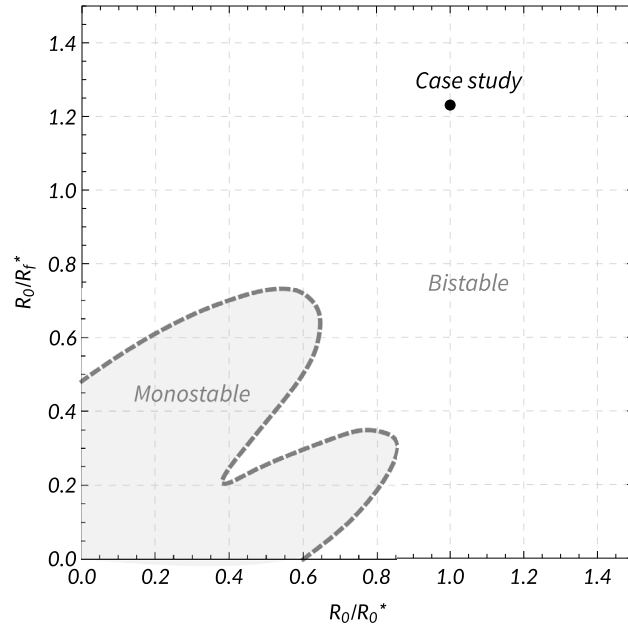


Fig. 5. Stability plot for varying pseudo radii R_0^* and R_f^* projected on the planes ρ_1 and ρ_2 .

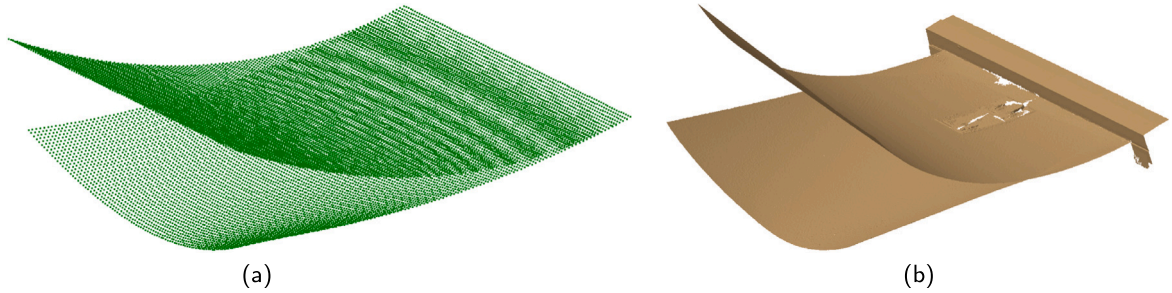


Fig. 6. Morphing diagrams: (a) analytical prediction and (b) bench tests based on point clouds.

For the chosen material properties and aspect ratio, Fig. 5 shows the mono- (light gray) and bistability (white) domains of the clamped shell in the plane of the dimensionless initial curvatures.

The highlighted point in Fig. 5 corresponds to analytical prediction (see Fig. 6a) and the manufactured prototype (see Fig. 6b); according to the model, once clamped, the prototype shell exhibits the two stable equilibrium configurations I and C shown in Fig. 7. Albeit strictly referred to static bistability, the analytical prediction confirms that the experimental shell configuration is far from the monostable boundary. Note that the reduced analytical model predicts a static equilibrium states which may differ from dynamic steady states.

3. Experimental research

This section presents the study of the cantilever shell dynamics and the analysis of the experimental results. The tests are performed on an electrodynamic shaker — with maximum dynamic load 35 kN. The head expander is attached to the shaker armature and it is the base for shell clamping. The tested shell is clamped at a distance 180 mm from its free end. On such a mounted structure the strain gauge and piezoelectric element are embedded. The latter component is the so-called Macro Fiber Composite (MFC) patch; the piezoelectric element $M2814 - P1$ with $d33$ piezoelectric effect is selected [36]. This choice was preceded by a series of preliminary tests. It was observed that large size MFC patches, which would provide more efficient energy harvesting, affects significantly the shell mechanical properties and might prevent bistable behavior. Therefore, a small size and highly flexible MFC patch is selected. $P1$ element was preferred to the more common $P2$ one because the different set of the electrodes in $P2$ type elements can be easily damaged even for small shell vibration.

The MFC patch is glued to the shell longitudinal symmetry axis at a distance of 25 mm from the clamping. On the opposite side of the shell a strain gauge with dimensions of about 5×4 mm and resistance 120 Ω is glued. The strain gauge placement corresponds to the center of MFC patch.

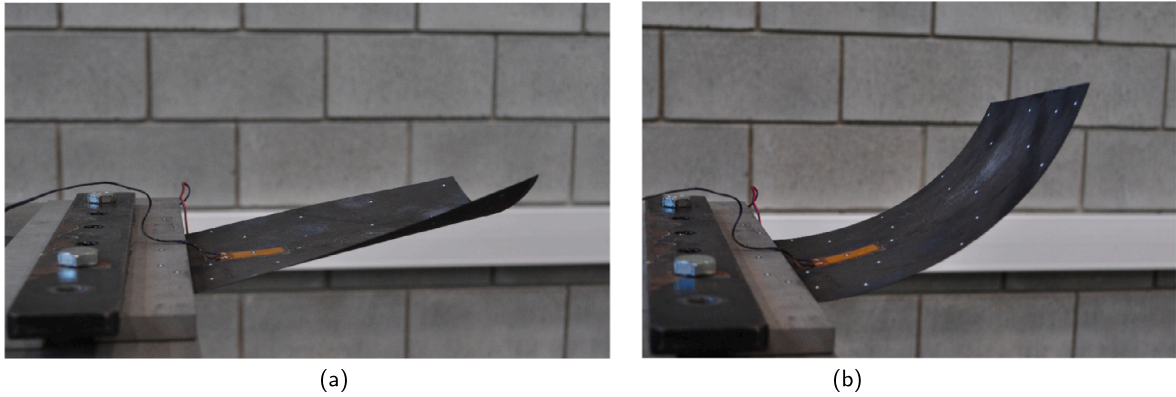


Fig. 7. Equilibria of shell's prototype: (a) *I* shape and (b) *C* shape.

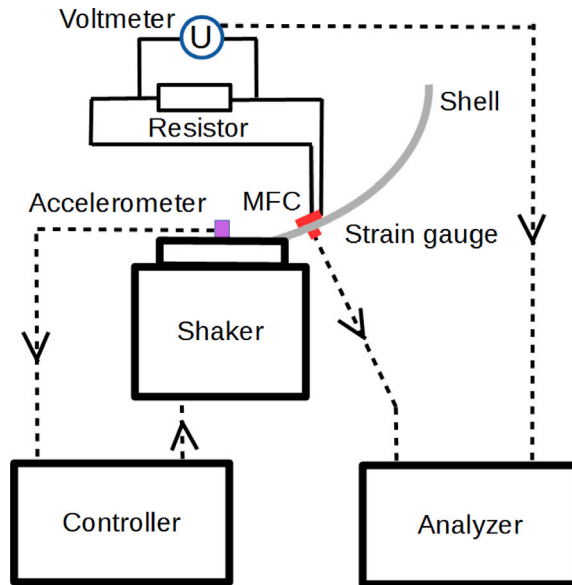


Fig. 8. Diagram of the measuring system.

The MFC patch and the strain gauge allowed to measure the level of recovered energy and the shell vibration, respectively. The shaker operation and the signals recording is supported by the analyzer with the dedicated software (see Fig. 8). An additional accelerometer and feedback control allowed controlling the shaker motion.

During a single test, the acceleration amplitude of shaker armature is constant whereas, frequency of excitation is changed linearly (sweep mode — linear) with a constant sweep rate 0.01 Hz/s. The frequency is swept forward and backward from 5 Hz to 9 Hz. The excitation signal is defined in the following form:

$$a(t) = a_S \sin \left(\omega_1 t + \frac{1}{2} \alpha t^2 \right), \tag{3}$$

where $a(t)$ is the shaker armature acceleration, a_S is constant amplitude, and $\alpha = \frac{\omega_2 - \omega_1}{\Delta t}$ with ω_1, ω_2 initial and final sweep frequency, respectively and Δt is test time.

3.1. Experimental analysis of shell dynamics

The sine tests are performed for several excitations levels with fixed values of amplitude: 0.1 g, 0.2 g, 0.4 g, 0.6 g, 0.8 g, 1 g, 1.2 g, 1.4 g, 1.6 g, 1.8 g, where g is gravity acceleration. The tested shell has two stable equilibrium positions, so-called *I* and *C*. The configurations *I* or *C* are taken as the shell initial shape during a single test with a forward or backward frequency sweep. Four tests for each amplitude level were carried out: a sweep forward starting from *I* and *C* state and a sweep backward starting from *I* and *C* state. In the remainder, to label each simulation, a notation including information about the initial shell configuration, the

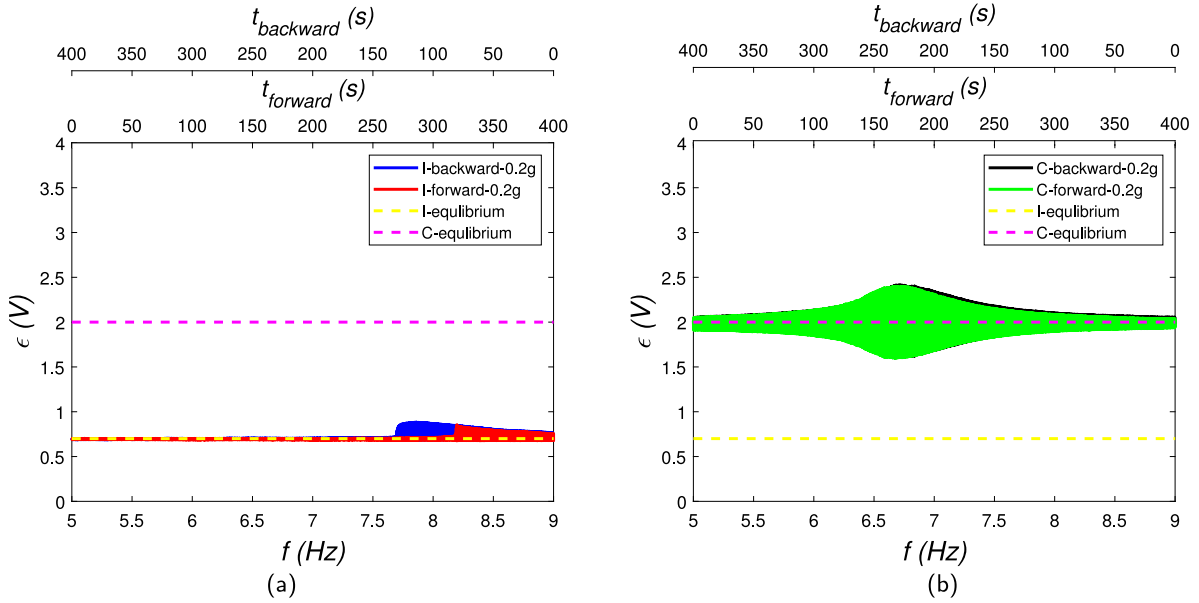


Fig. 9. Time series of shell strain for excitation amplitude 0.2 g: (a) initial *I* shape and (b) initial *C* shape. (For interpretation of the references to color in this figure legend, the reader is referred to the web version of this article.)

frequency sweep direction and the excitation amplitude level is introduced. For example for $a_s = 0.1$ g the notation is: *I*-forward-0.1 g, *I*-backward-0.1 g, *C*-forward-0.1 g, *C*-backward-0.1 g. During all tests, an electrical circuit with resistor is connected to the MFC element.

The linear sweep correlates the value of excitation frequency (given in rad/s or Hz) and time (in seconds):

$$\omega(t) = \omega_1 + \alpha t \quad \text{or} \quad f(t) = f_1 + \frac{\alpha}{2\pi} t, \tag{4}$$

where $f_1 = 5$ Hz, $\alpha/2\pi = 0.01$ Hz/s for the frequency sweep forward or $f_1 = 10$ Hz, $\alpha/2\pi = -0.01$ Hz/s for the frequency sweep backward.

Figs. 9 and 10 present time series of shell strain ϵ for small and large excitation levels: $a_s = 0.2$ g and $a_s = 1.8$ g. The time series for sine tests have been plotted for frequency sweep forward and backward in time domains ($t_{forward}$, $t_{backward}$) indicated in the top axes. Based on Eq. (4) both time axes are related to the bottom axis of the frequency sweep. This procedure enables a direct and fast comparison of the obtained time responses.

The strain gauge was calibrated for the free shell, i.e. before clamping. During clamping the initial deformations are confirmed by strain gauge indications. The initial strain for each equilibria are marked by horizontal dashed lines, 0.7 V indicates *I* equilibrium and 2 V corresponds to *C* equilibrium. Time series with respect to *I* equilibrium are asymmetric (Fig. 9a) with a clear amplitude jump. The localization of the amplitude jump indicates the softening phenomenon of the resonance curve. The existence of softening at small vibrations indicates that it is a strong effect and that the natural frequency for *I* mode is strongly amplitude dependent. The shell behaves differently for the *C* initial shape. Small shell vibrations are symmetrical around *C* equilibrium (Fig. 9b) and the response is close to a linear system. In both cases described above the vibrations are only around one equilibrium. This type of dynamics is called in-well or local dynamics. Whereas, when the vibration can reach both equilibria the motion is referred to as cross-well or global dynamics. The possibility of the jump between equilibria is referred to as snap-through effect. For small excitation the snap-through between both equilibria is not observed. The snap-through of the oscillation from *I* equilibrium to *C* equilibrium and vice versa requires larger excitation.

Fig. 10 shows more complex system dynamics. For larger excitation level and *I* initial shape, two different scenarios are identified (Fig. 10a). The first scenario, plotted in red, refers to forward frequency sweep. Local oscillations around *I* equilibrium are observed from 5 Hz up to 5.2 Hz. Local oscillations around *C* equilibrium are then observed from 5.2 Hz up to 5.8 Hz. Snap through effect occurs from 5.8 Hz up to 6.7 Hz. Vibration around *C* equilibrium are again observed from 6.7 Hz up to 9 Hz. The second scenario, indicated by blue series, refers to backward frequency sweep. Local oscillations around *I* equilibrium are observed from 9 Hz up to 8.4 Hz. Local oscillations around *C* equilibrium are then observed from 8.4 Hz up to 6.7 Hz. Snap through effect occurs from 6.7 Hz up to 5.8 Hz. Vibration around *C* equilibrium are again observed from 5.8 Hz up to 5 Hz. Analyzing both scenarios for forward and backward sweep we may conclude that for the same excitation frequency more than one solution can exist. For *C* initial shape three areas are identified (Fig. 10b). For forward sweep and frequency domains from 5 Hz to 5.8 Hz and from 6.7 Hz to 9 Hz, local vibrations around *C* equilibrium take place. Between frequency 5.8 Hz and 6.7 Hz the snap-through effect occurs. In this frequency domain the maximum of the response is above *C* equilibrium and the minimum of the response is below *I* equilibrium. Similar time series are obtained for forward and backward frequency sweep.

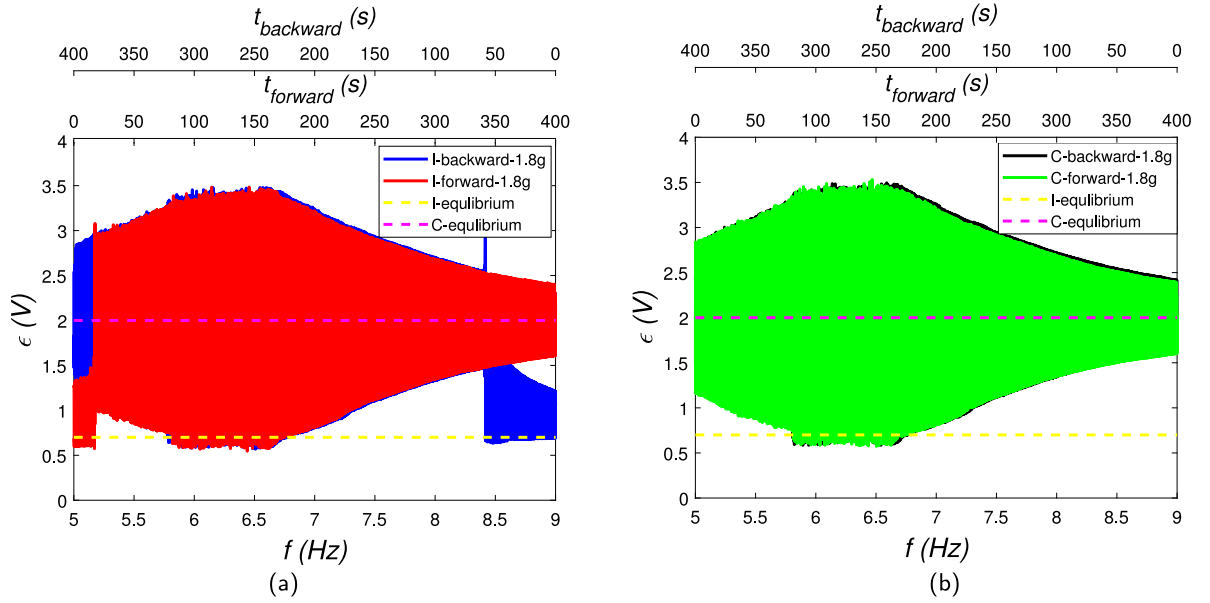


Fig. 10. Time series of shell strain for excitation amplitude 1.8 g: (a) initial *I* shape and (b) initial *C* shape. (For interpretation of the references to color in this figure legend, the reader is referred to the web version of this article.)

The shell's strain response can be described in the form:

$$\epsilon(t) = \epsilon_0 + \epsilon_1 \sin(\omega t + \varphi) + OOH, \quad (5)$$

where ϵ_0 is a constant term, which corresponds to vibration offset, ϵ_1 is the amplitude of the harmonic term with excitation frequency ω and φ is the shift in phase. *OOH* stands for the Other Order Harmonics, i.e. subharmonics and superharmonics. Time histories are processed by means of commercial software LMS to determine the amplitude of harmonic component ϵ_1 assigned to a given amplitude and frequency of excitation $a_S(\omega)$. Frequency–amplitude curves are gathered in Figs. 11 and 12.

The resonance characteristics recorded for various excitation levels show better the variability of the tested shell dynamics. An involved dynamics is presented in Fig. 11 for vibrations around *I* equilibrium. For small excitation levels - from 0.1 to 0.6 g the maxima of the resonance curves shift significantly towards lower frequencies. The approximate backbone curve (blue color) shows that the change in resonant frequency is about 1.4 Hz. This confirms the existence of strong softening effect for *I* configuration. Whereas, for larger excitation amplitudes ($a_S > 0.6$ g) the jump from regular oscillations around *I* equilibrium to regular oscillations around *C* equilibrium is visible. Following the curves of the same color in Fig. 11 (e.g. yellow) one can find zones, where two different amplitudes exist for a given excitation frequency (dashed and solid lines do not overlap). In these zones larger amplitude values correspond to vibrations around *C* equilibrium, while lower amplitude ones to vibration around *I* equilibrium. The forward frequency sweep show jumps from *I* vibration to *C* vibration corresponding to the vertical lines in Fig. 11. The beginning of the jumps (bottom of the vertical lines) always correspond to the shell amplitude ϵ_1 about 0.35 V. The transition of the dashed line from vibrations around *I* to *C* is accompanied by a zone with a non-smooth curve. These sudden changes of the response occur after the period doubling bifurcation as it will be proved in the next paragraph.

For *C* initial shape (Fig. 12) and excitation amplitude varying from 0.1 g to 1.2 Hz local oscillations around *C* equilibrium are observed. These frequency–amplitude curves are smooth and represent regular motion. The peak of curves for $a_S = 0.1$ g occurs for frequency 6.8 Hz, which can be taken as the linear natural frequency for *C* vibration mode. The maxima of curves for higher excitations shift towards lower frequencies. The obtained trend is marked in blue and it approximates the backbone curve which is close to linear. This results indicates a weak softening effect with a change in resonant frequency of about 0.4 Hz. For larger excitation amplitudes ($a_S > 1.2$ g) the zone where the resonance curves lose smoothness is visible. These significant changes of amplitude ϵ_1 can be identified as the result of the snap-through effect (see above the description of zones in Fig. 10). The harmonic estimator related only to the excitation frequency displays limitations for presented frequency response curves, in particular Figs. 11 and 12 disclose discontinuous areas. The time series confirm irregular amplitude fluctuations which involve more complex dynamic effects. For example, nonlinear couplings stimulate higher order modes, while the snap-through oscillations cause the value of the harmonic amplitude ϵ_1 to vary irregularly in successive estimation steps as well as rapid motion activates multiple harmonic response. Better identification of these effects have been presented in next section.

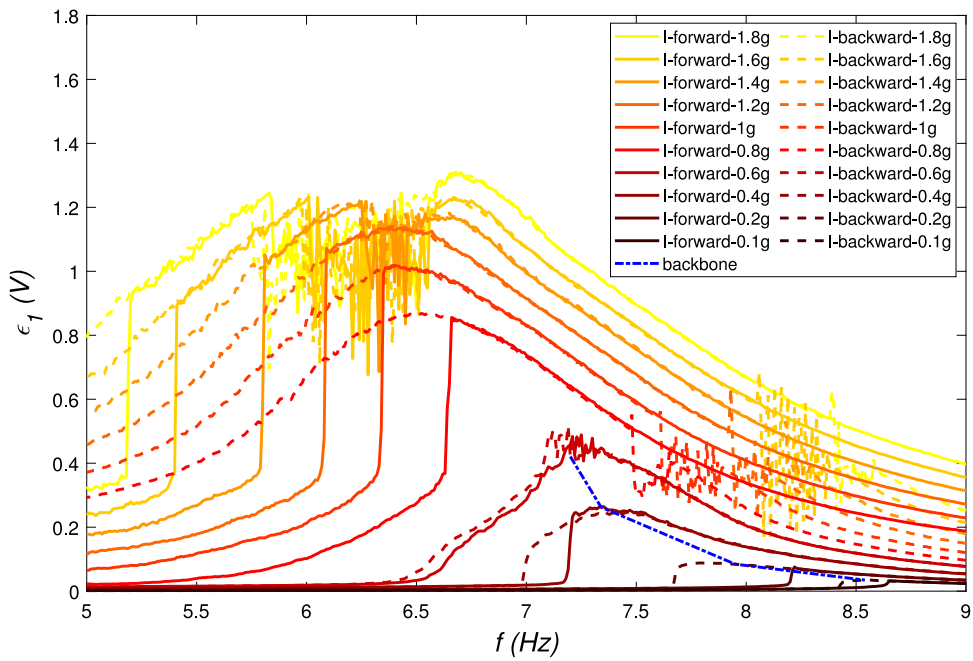


Fig. 11. The resonance characteristics for *I* initial shape and selected amplitudes of excitation. (For interpretation of the references to color in this figure legend, the reader is referred to the web version of this article.)

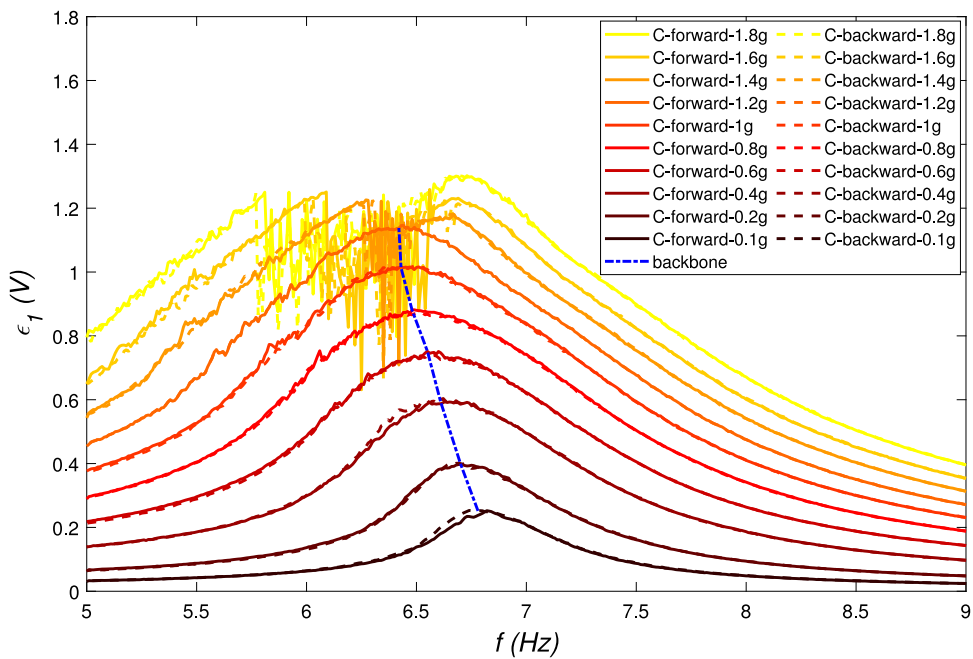


Fig. 12. The resonance characteristics for *C* initial shape and selected amplitudes of excitation. (For interpretation of the references to color in this figure legend, the reader is referred to the web version of this article.)

3.2. Qualitative analysis of shell vibrations

The standard procedure applied for automatic recording of resonance curves is insufficient in this case. Therefore, additional criteria to identify the different kind of shell motion are proposed. We refer to a specific example to make clear the procedure.

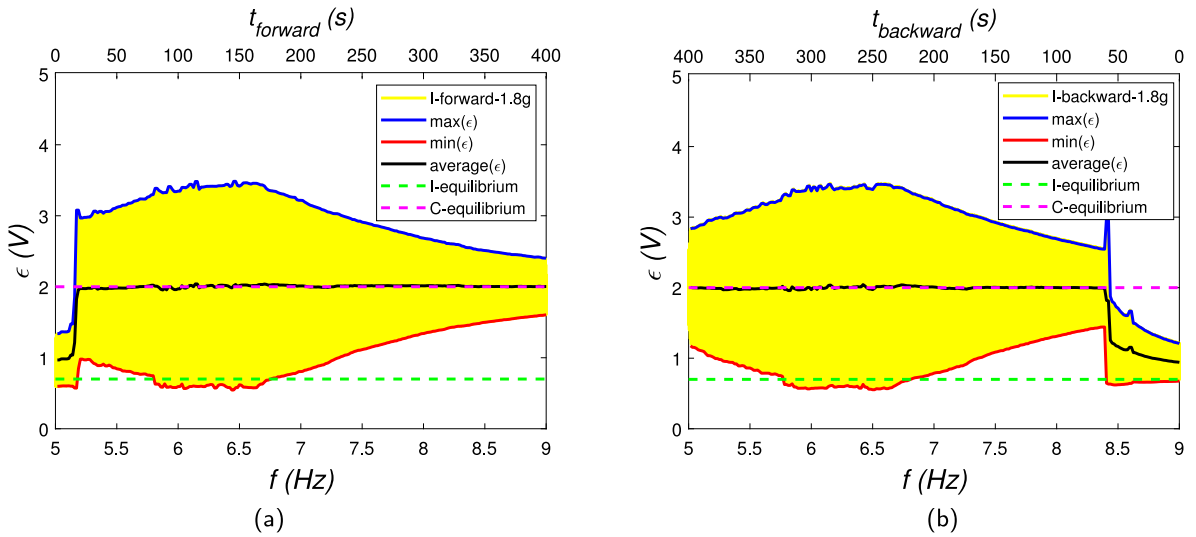


Fig. 13. Time series of the shell strain and its statistic parameters for excitation amplitude 1.8 Hz and I initial shape: (a) frequency sweep forward and (b) frequency sweep backward. (For interpretation of the references to color in this figure legend, the reader is referred to the web version of this article.)

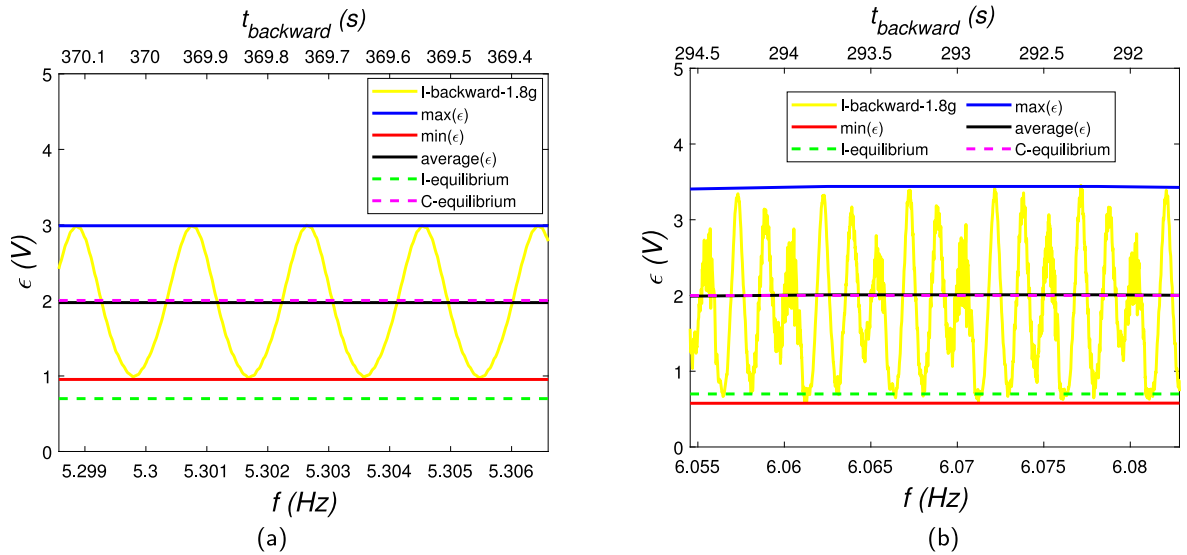


Fig. 14. Zoom of time series for selected parameters: (a) C -regular vibration and (b) $snap$ -through vibration. (For interpretation of the references to color in this figure legend, the reader is referred to the web version of this article.)

Fig. 13 shows the time series of the shell strain for forward and backward frequency sweeps recorded at an excitation amplitude of 1.8 g, along with the strain values $\epsilon_I \approx 0.7$ V and $\epsilon_C \approx 2$ V corresponding to the stable equilibria I and C .

The figure also report the maximum, ϵ_{max} , minimum, ϵ_{min} , and average, ϵ_{avg} , values of the shell strain, determined from short time windows continuously moving throughout time domain of the test. As we will show, these quantities make it possible to distinguish the four different types of motion that we have experimentally identified: (i) a periodic in-well motion around the C stable configuration (C -regular); (ii) a cross-well reversible $snap$ -through motion ($snap$ -through); (iii) a 1 : 1 periodic in-well motion around the I stable configuration (1 : 1- I -regular); (iv) a 2 : 1 periodic in-well motion around the I stable configuration (2 : 1- I -regular).

To this aim, we first observe that C -regular and $snap$ -through motions occur whenever the average strain ϵ_{avg} is greater than a limit value $\hat{\epsilon} \approx 1.5$ V. In particular, for $\epsilon_{avg} > \hat{\epsilon}$, C -regular motion occurs when the minimum strain is greater than the strain value corresponding to the I stable configuration, $\epsilon_{min} > \epsilon_I$, Fig. 14a, whereas for $\epsilon_{min} \leq \epsilon_I$ the $snap$ -through motion takes place, Fig. 14b.

Periodic in-well motions around the I stable configuration occur for $\epsilon_{avg} \leq \hat{\epsilon}$. Then, 1 : 1- I -regular and 2 : 1- I -regular motions can be distinguished on the basis of the ratio between the areas above and below the average strain value, that is, by the “level of

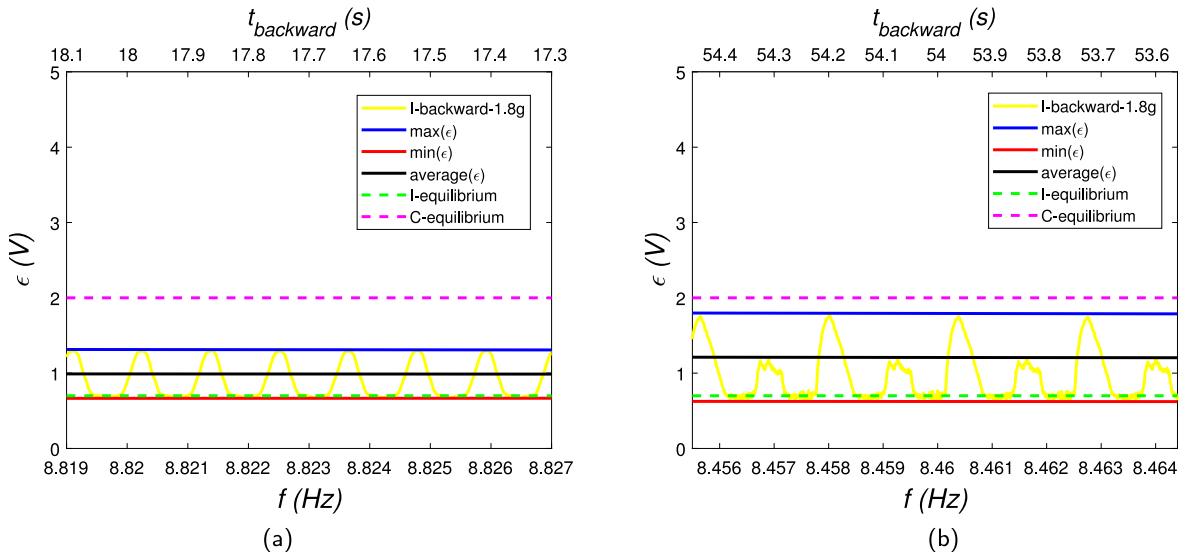


Fig. 15. Zoom of time series for selected parameters: (a) I -regular vibration and (b) I -regular vibration with period doubling. (For interpretation of the references to color in this figure legend, the reader is referred to the web version of this article.)

symmetry” of the strain time history with respect to ϵ_{avg} . Thus, by defining the indicators

$$A_{top} := \sum_{j=1}^n |\epsilon_j - \epsilon_{avg}|, \quad \text{where} \quad \begin{cases} \epsilon_j = \epsilon_j & \text{if } \epsilon_j \geq \epsilon_{avg} \\ \epsilon_j = 0 & \text{if } \epsilon_j < \epsilon_{avg} \end{cases} \quad (6)$$

and

$$A_{bot} := \sum_{j=1}^n |\epsilon_j - \epsilon_{avg}|, \quad \text{where} \quad \begin{cases} \epsilon_j = \epsilon_j & \text{if } \epsilon_j < \epsilon_{avg} \\ \epsilon_j = 0 & \text{if } \epsilon_j \geq \epsilon_{avg} \end{cases} \quad (7)$$

n being the total number of points in the time window, we find that the 1 : 1- I -regular motion occurs for $A_{top}/A_{bot} < 4$, Fig. 15a, and the 2 : 1- I -regular motion occurs for $A_{top}/A_{bot} \geq 4$, Fig. 15b. In Fig. 15, A_{top} is proportional to the area above the black line and below the yellow line, A_{bot} to the area below the black line and above the yellow line.

All in all, the criterion distinguishing the different types of motion can be written in the following form:

$$\begin{cases} \epsilon_{avg} > \hat{\epsilon} & \begin{cases} \epsilon_{min} > \epsilon_I & C\text{-regular} \\ \epsilon_{min} \leq \epsilon_I & \text{snap-through} \end{cases} \\ \epsilon_{avg} \leq \hat{\epsilon} & \begin{cases} A_{top}/A_{bot} < 4 & 1 : 1\text{-}I\text{-regular} \\ A_{top}/A_{bot} \geq 4 & 2 : 1\text{-}I\text{-regular} \end{cases} \end{cases} \quad (8)$$

Based on criterion (8), two color maps – amplitude of excitation against excitation frequency – are plotted in Fig. 16 considering: I -forward, I -backward, C -forward and C -backward sweeps. Fig. 16a refers to frequency sweeps starting from the I stable equilibrium, Fig. 16b to frequency sweeps starting from the C stable equilibrium. Orange regions correspond to C -regular motions, brown regions correspond to snap-through motions, blue regions correspond to 1 : 1- I -regular motions and green regions correspond to 2 : 1- I -regular motions.

The map in Fig. 16a shows a mix of both I -forward and I -backward scenarios. For the I -forward scenario the orange color would be extended to the map’s right end, whereas, for the I -backward one, the situation would be the opposite, i.e. the orange color would be continued to the map’s left end. As shown, forward and backward scenarios show a different arrangement of I vibration regions (blue and green color). The map in Fig. 16b shows the overlapping scenarios relevant to C -forward and C -backward frequency sweeps.

Therefore, for a given combination of frequency and amplitude, if the colors in the two maps coincide, one solution exists, while if the colors differ two solutions are possible. In essence, these maps summarize all kinds of detected motion with respect to the explored range of amplitude and frequency of excitation.

Two regions with single solution are detected: the brown zone with only snap-through motion and the orange zone only with C -regular motion. Areas with two solutions, one related to C -regular motions, and second related to I -regular motions, are shown by blue and green areas in Fig. 16a and by orange areas in Fig. 16b.

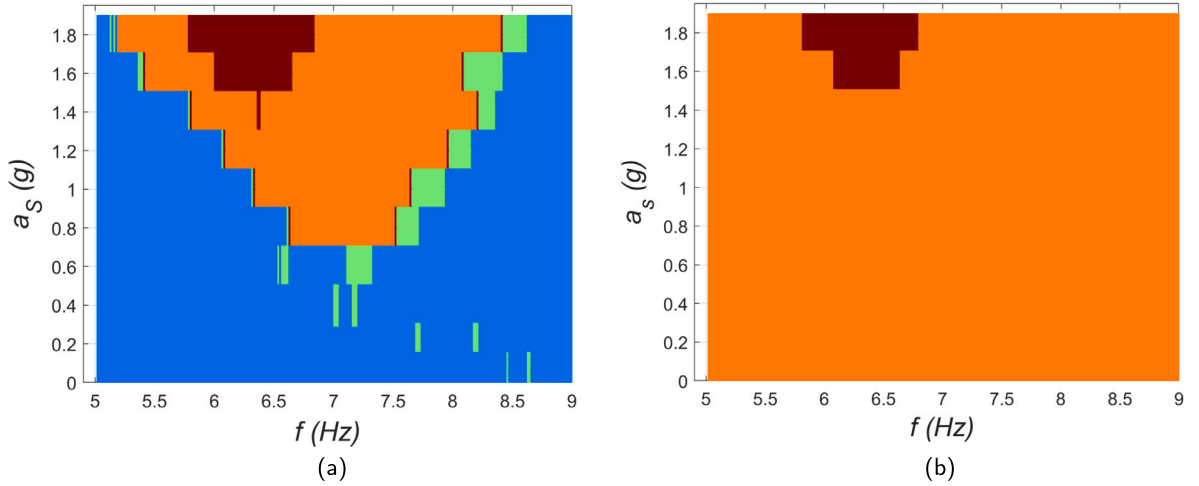


Fig. 16. Two parameters maps — amplitude of excitation against excitation frequency with indicated different kind of motion: (a) *I* initial shape and (b) *C* initial shape. Notation of motion based on criterion (8): *C-regular* - orange color, *snap-through* - brown color, 1:1-*I-regular* - blue color, 2:1-*I-regular* - green color. (For interpretation of the references to color in this figure legend, the reader is referred to the web version of this article.)

The proposed criterion may generate some minor imperfections on the plotted maps when the dynamic regime changes abruptly: some small green zones visible in blue areas, brown zones between green and orange regions or blue and orange regions, result from jumps between *I-regular* and *C-regular* motions.

The derived dynamic regimes' mapping will be exploited in Section 4 to gain insights on the level of the energy recovery efficiency provided by the bistable shell.

3.3. Analysis of FFT and Poincaré maps

The analysis of experimental results presented in previous section shows three dynamic regimes: periodic oscillations with period T , after the period doubling bifurcation with period $2T$, and *snap-through* motion. The existence of various kinds of motion can be confirmed by FFT analysis and Poincaré maps. So, additional experimental tests are carried out for constant excitation frequency and varying excitation amplitudes. Each step with a constant excitation amplitude is initiated for the assumed shell shape applying so-called startup time. This time is used to change the shell shape so that during each step the initial shape is fixed in *I* equilibrium. Based on Fig. 16a two excitation frequencies are selected - 6.4 Hz and 8.3 Hz. These cases are important because for 6.4 Hz the motion should be changed from *I* vibration to *C* vibration and then to the *snap-through* effect. For 8.3 Hz the transition from *I* vibration with 1:1 to 2:1 ratio between response and excitation period and finally to the transition to *C* vibration is investigated. Fig. 17 shows the experimental results, which demonstrates this scenario.

To create a phase portrait or Poincaré map the velocity of the measured signal is needed. Since this variable is not directly measured, it is reconstructed by a phase shift of the measured strain $\epsilon(t + \tau)$. If the measured signal is periodic (e.g. given as sine function) the reconstructed velocity signal should be shifted by phase $\pi/2$. The value of time delay can be determined from the analysis of following relationships:

$$\epsilon(t) = A \sin(\omega t), \quad (9)$$

and

$$\epsilon_\tau = \epsilon(t + \tau) = A \cos(\omega t) = A \sin\left(\omega t + \frac{\pi}{2}\right) = A \sin\left[\omega\left(t + \frac{\pi}{2\omega}\right)\right] = A \sin[\omega(t + \tau)], \quad (10)$$

where time delay takes value $\tau = \pi/(2\omega)$. Using this approach the phase portrait and Poincaré maps are determined in Fig. 18.

The analysis of the evolution of phase portraits and Poincaré maps clarifies the change of motion scenarios. For the frequency 6.4 Hz (see Fig. 18a), the first two orbits correspond to very small vibrations. Interestingly enough, this dynamics shows some analogies with another case previously analyzed by the authors, i.e. a preloaded pendulum with a bumper [37]. In both systems, either the tested shell or mentioned pendulum with bumper, the oscillation have similar nature. This means that for *I* shape the shell in one direction has very large stiffness, corresponding to the mentioned bumper, and in opposite direction its stiffness is much smaller. The third phase portrait shows regular vibrations around *I* equilibrium. These vibrations for *I* mode are similar to the impacts of the mentioned pendulum against a bumper. The Poincaré map has one point. Therefore, the oscillation period is equal to the excitation period. For a_s about 0.8 g there is a jump to regular vibrations around *C* equilibrium. The phase portrait takes an ellipse shape with a single point on Poincaré map. The presented successive ellipses get larger and larger until the signal exceeds the *I* equilibrium value. Then, the *snap-through* mechanism is activated. The last three maps represent this phenomenon. The shape

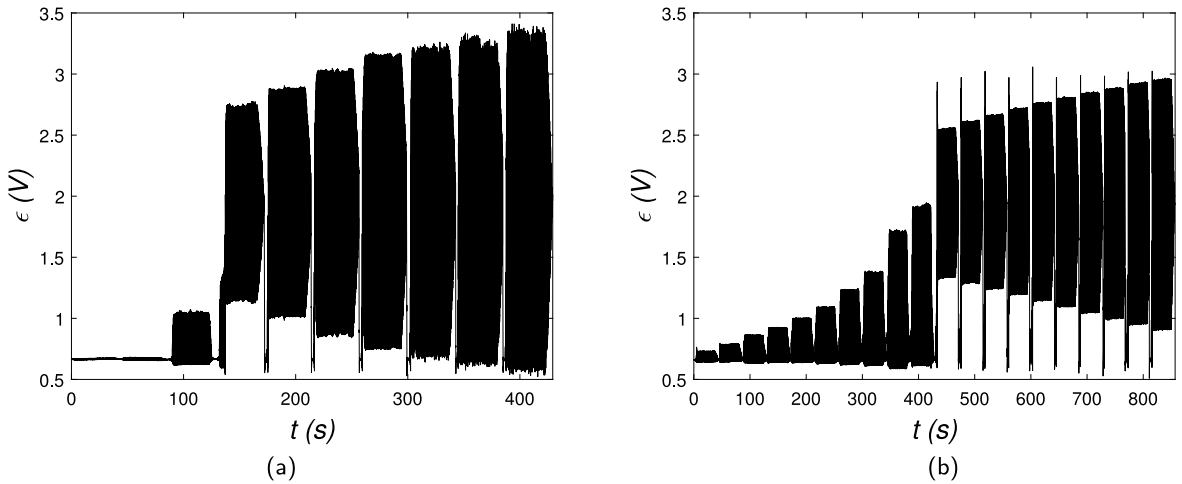


Fig. 17. Steps test: (a) excitation frequency 6.4 Hz, excitation amplitude varied from 0.18 g to 1.8 g with step 0.18 g and (b) excitation frequency 8.3 Hz, excitation amplitude varied from 0.18 g to 3.6 g with step 0.18 g.

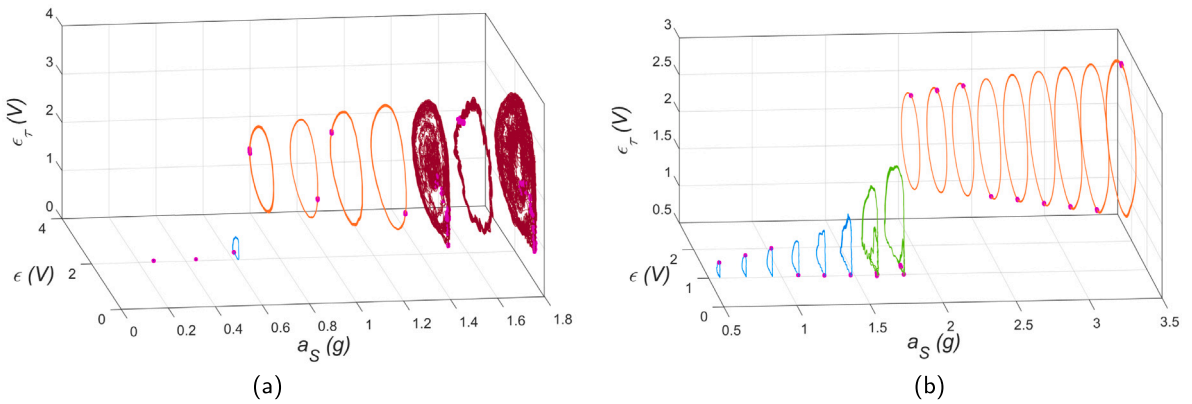


Fig. 18. Phase portraits (solid lines) and Poincaré maps (points of the projected trajectory) from steady state of the steps test: (a) excitation frequency 6.4 Hz, excitation amplitude varied from 0.18 g to 1.8 g with step 0.18 g and (b) excitation frequency 8.3 Hz, excitation amplitude varied from 0.54 g to 3.42 g with step 0.18 g. Notation of motion based on criterion (8): *C-regular* - orange color, *snap-through* - brown color, *1 : 1-I-regular* - blue color, *2 : 1-I-regular* - green color. (For interpretation of the references to color in this figure legend, the reader is referred to the web version of this article.)

of phase portrait confirms earlier suppositions that for the *snap-through* both either regular or chaotic responses may occur. For a_S about 1.44 g and 1.8 g the phase portraits have strange attractors, which are typical for chaotic oscillations. Between them there is a trajectory of regular motion. In the second considered scenario, shown in Fig. 18b, the dynamics seem to be simpler. All phase portraits present regular motion. The first eight trajectories are related to oscillations around *I* equilibrium. Whereas, next nine trajectories represent regular oscillations around *C* equilibrium. However, for the last two *I* vibration trajectories, before the jump additional loops on the phase portraits occur. This result indicates the period doubling bifurcation. The response period is twice larger than excitation period (2 : 1) and this is clearly indicated by two points on Poincaré maps. The same effect can be found in the referred paper, where preloaded pendulum with a bumper was investigated. This may indicate that the shell vibrations around *I* equilibrium have a similar mechanism to the soft impact system.

The analysis of phase portraits and Poincaré maps is extended by FFT analysis. In Eq. (5) it is emphasized that other harmonics i.e. subharmonics and superharmonics may occur in the response. The analysis carried out in the frequency domain completes the information about additional harmonics of amplitude ϵ_j . The spectra presented in Fig. 19 are computed for the steady states as in Fig. 17. The largest amplitude in all spectra corresponds to excitation frequency. In most cases the response is composed of higher harmonics, for example:

$$\epsilon(t) = \epsilon_0 + \epsilon_1 \sin(\omega t + \varphi_1) + \epsilon_2 \sin(2\omega t + \varphi_2) + \epsilon_3 \sin(3\omega t + \varphi_3) + \dots, \tag{11}$$

where ϵ_2, ϵ_3 are amplitudes of higher harmonics.

With the help of the frequency analysis the period doubling and chaotic oscillation are detected. In Fig. 19a the curves for $a_S = 1.44$ g and $a_S = 1.8$ g confirm irregular motion. These spectra have a few dominating amplitude peaks, but with coexisting

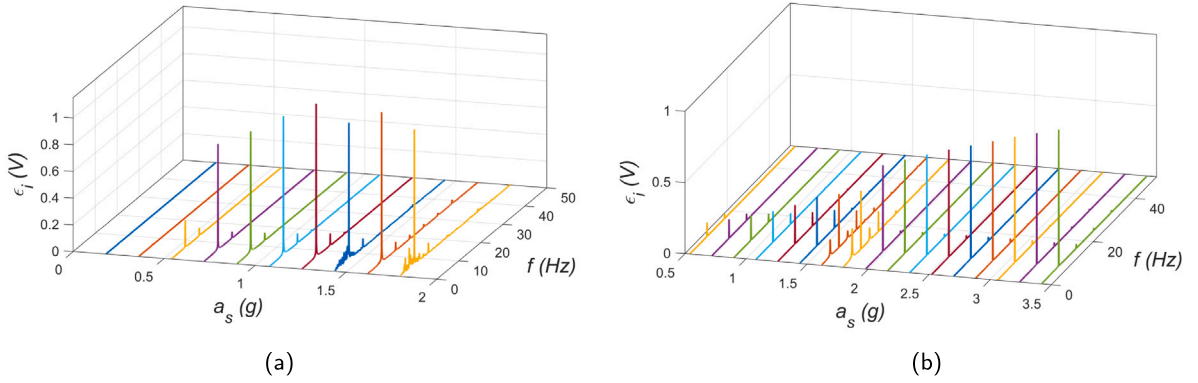


Fig. 19. FFT diagram for steady state of the step test: (a) excitation frequency 6.4 Hz, excitation amplitude varied from 0.18 g to 1.8 g with step 0.18 g and (b) excitation frequency 8.3 Hz, excitation amplitude varied from 0.54 g to 3.42 g with step 0.18 g. (For interpretation of the references to color in this figure legend, the reader is referred to the web version of this article.)

many other spread peaks. This fact confirms that this response is chaotic. In Fig. 19b for $a_s = 1.62$ g and $a_s = 1.8$ g the period doubling effect is confirmed. The curves for these responses have additional components occurring with fractions of the excitations frequency. For example:

$$\epsilon(t) = \epsilon_0 + \epsilon_{1/2} \sin\left(\frac{1}{2}\omega t + \varphi_{1/2}\right) + \epsilon_1 \sin(\omega t + \varphi_1) + \epsilon_{3/2} \sin\left(\frac{3}{2}\omega t + \varphi_{3/2}\right) + \epsilon_2 \sin(2\omega t + \varphi_2) \dots \quad (12)$$

where $\epsilon_{1/2}$, $\epsilon_{3/2}$ are amplitudes of subharmonics. The period doubling may appear in the studied system on the border of occurrence of *I-regular* and *C-regular* solutions before the jump from *I* oscillations to *C* oscillations.

4. Effectiveness of energy recovery

As presented in the previous chapter the dynamics of the shell is complex. From the energy recovery point of view, it is important to determine the kind of motion which will generate the largest amount of energy. The previously described premises determined the choice of the MFC patch. For the energy recovery an electrical circuit with resistor having resistance $R = 400$ k Ω is connected to MFC patch. This choice is preceded by preliminary tests to find the resistance value to optimize the measured voltage U . The power P is determined from the relationship:

$$P = \frac{U^2}{R}. \quad (13)$$

The influence of the kind of motion on the efficiency of energy recovery can be determined by calculating the RMS value of electrical power in a time window:

$$P_{RMS} = \sqrt{\frac{1}{n} \sum_{j=1}^n P_j^2} = \sqrt{\frac{1}{n} \sum_{j=1}^n \left(\frac{U_j^2}{R}\right)^2} \quad (14)$$

where index j is the point number from the analyzed time window whereas n is related to the total length of window's time domain. Finally, computing power defined by Eq. (14) the color maps showing the power RMS for amplitude and frequency of excitation are presented. The obtained maximum recovered energy is equal to 0.0433 mW.

The maps have been obtained using mesh MATLAB function. They are presented in Fig. 20 and correspond to maps of the motion types (Fig. 16). Analyzing the color distribution on both maps, a very similar distribution is visible for the largest efficiency of energy recovery. The localization and shape of the zone with mixed red and brown colors (similar to a triangle) are identical on both maps. Based on Fig. 16, two kinds of motion can be attributed to this zone, i.e. *C-regular* vibration or *snap-through* motion. Maximum efficiency of energy recovery is achieved in the brown zone. The position of brown zone overlaps with the limit between two solution: *C* vibration and *snap-through* motion. Outside the triangle, there are zones of following colors: yellow, green, light and dark blue. The distribution of these colors are different for both maps. The color distribution of the map is more asymmetric in Fig. 20a. In this case, the transition from vibration around *I* to *C* equilibrium exists. The limit of this transition is asymmetric with respect to *snap-through* region. This is reflected in the mentioned asymmetric color distribution on the color map from Fig. 20a. A more symmetrical distribution is observed in Fig. 20b for vibrations with *C* initial shape. It is due to the fact that only *C-regular* oscillations can occur outside the *snap-through* region (Fig. 16b) and these vibrations have a nature close to linear (Fig. 12).

A closer view of the low amplitude harvesting performance is presented in Fig. 21. The excitation amplitude is limited to 0.6 g. For such low excitation amplitude only vibrations around *I* and *C* equilibrium appear on the maps, Figs. 21a and 21b, respectively. The color scale has also been modified to show differences for both kinds of motion. Now, the dark blue color corresponds to lack (negligible small) energy recovery. This zone is larger for vibrations around *I* equilibrium. Some similarity of *I* vibration to the

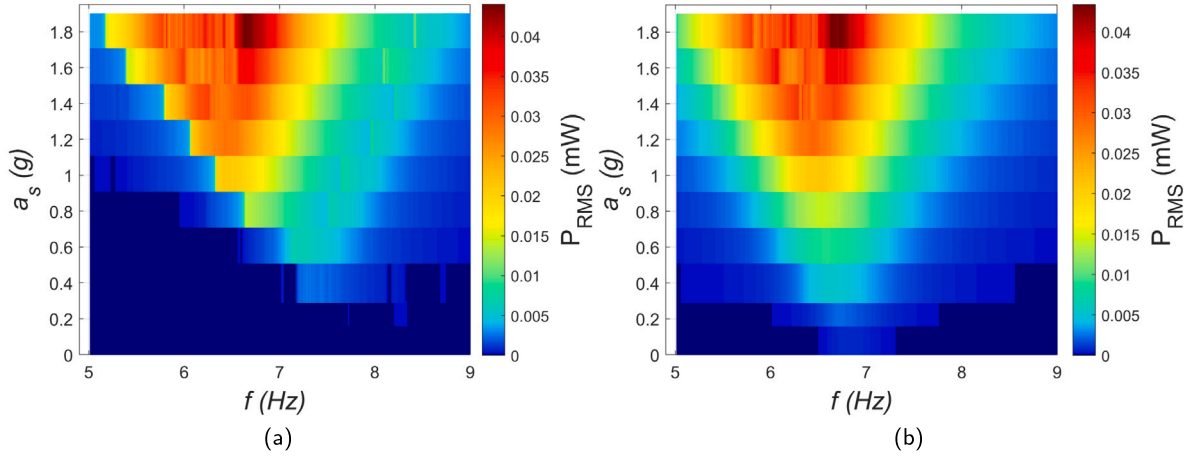


Fig. 20. Color maps for the full range of analysis. RMS of electrical power versus amplitude and frequency of excitation: (a) *I* initial shape and (b) *C* initial shape. (For interpretation of the references to color in this figure legend, the reader is referred to the web version of this article.)

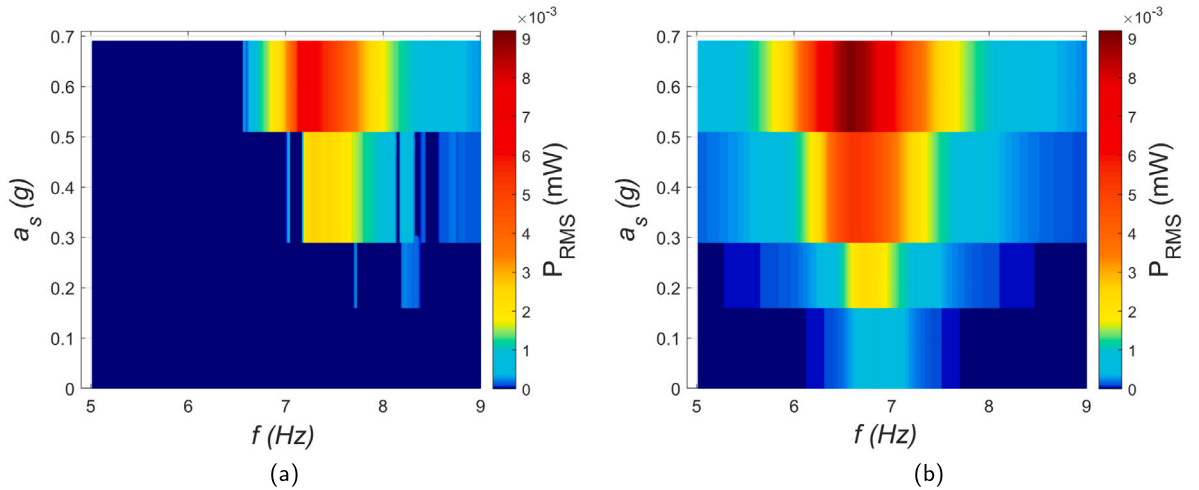


Fig. 21. Color maps for the full range of analysis. RMS of electrical power versus amplitude and frequency of excitation: (a) *I* initial shape and (b) *C* initial shape. (For interpretation of the references to color in this figure legend, the reader is referred to the web version of this article.)

system with impact and preload was mentioned earlier in this paper. This suggested preload effect can affect the large size of the dark blue region. For both kinds of motion a different maximum RMS of electrical power is observed. They are 0.0092 mW and 0.0066 mW for *C* and *I* vibration, respectively. In these conditions ($a_s \leq 0.6$ g) energy recovery from *C* vibration is about 40% larger than from *I* vibration.

All the considerations presented above indicate that more energy can be obtained from *C-type* or *snap-through* vibrations. However, the level of these vibrations (the measured shell strain) is usually larger than *I* oscillations. As a result, the interpretation of the energy recovery efficiency from different kinds of motion is not always directly linked to the type of motion. During energy harvesting, the direct piezoelectric effect is exploited. The piezoelectric material deformation (strain — the process input) generates electricity (electrical power — the process output). The efficiency can be described as ratio of output to input of the direct piezoelectric process. An index η is proposed in the form:

$$\eta = \frac{\sqrt{\frac{1}{n} \sum_{j=1}^n \left(\frac{U_j^2}{R} \right)^2}}{\sqrt{\frac{1}{n} \sum_{j=1}^n (\epsilon_j - \delta)^2}} \quad (15)$$

where RMS of the electrical power is in the numerator (see Eq. (14)) and RMS of measured strain in the denominator. The equation includes parameter δ , which eliminates the influence of the offset of the equilibrium position value (constant term) on the strain RMS value. The analysis of η index was performed for the cases presented in Figs. 14 and 15. These Figures present strain for all kinds of motion. Corresponding to them the time series of the obtained electric energy are shown in Figs. 22 and 23. For energy harvesting

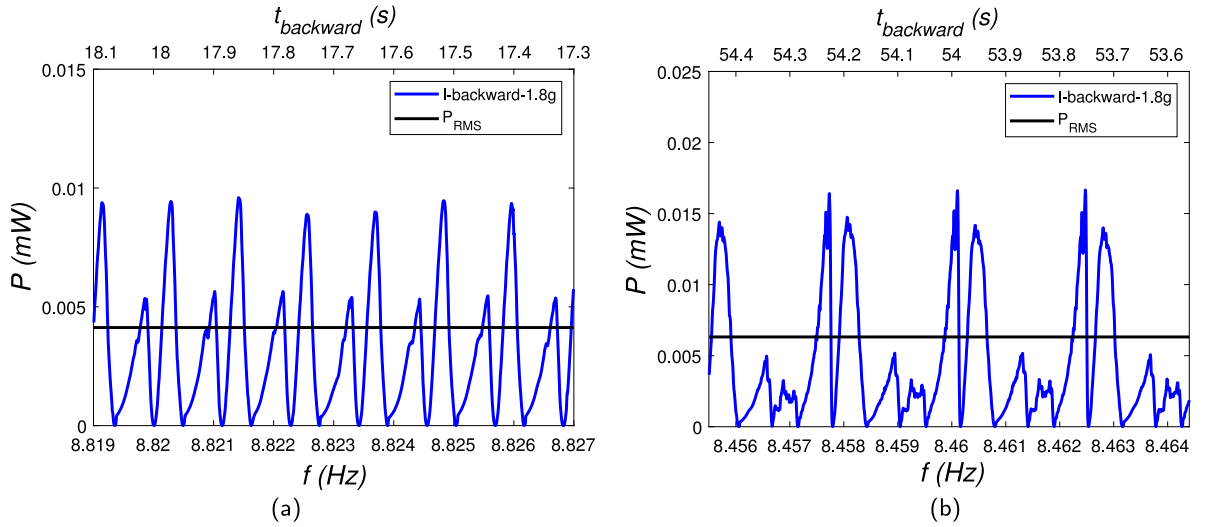


Fig. 22. Electrical power: (a) *I*-regular vibration and (b) *I*-regular vibration with period doubling. (For interpretation of the references to color in this figure legend, the reader is referred to the web version of this article.)

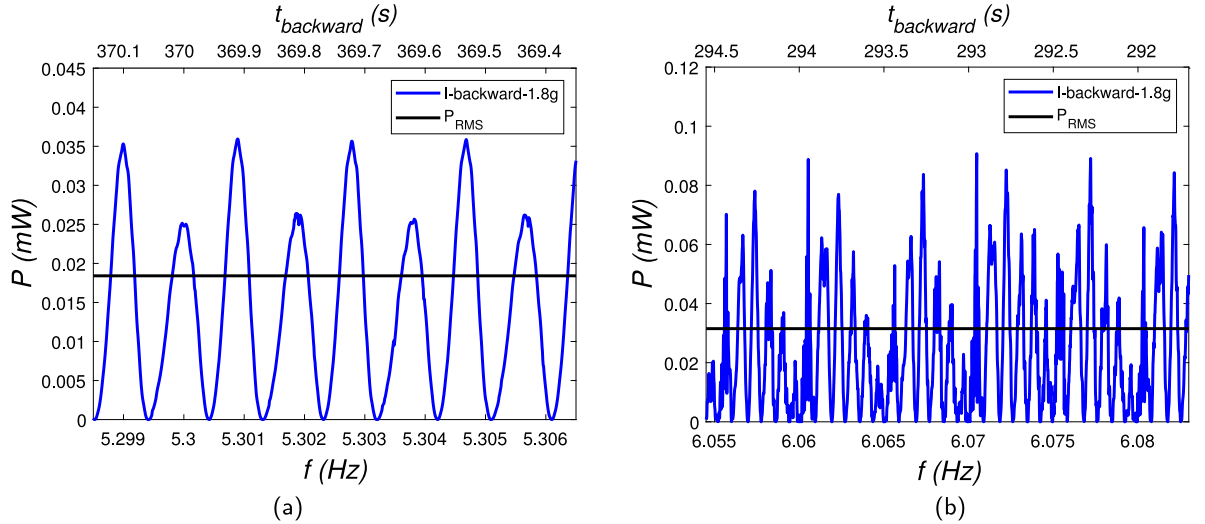


Fig. 23. Electrical power: (a) *C*-regular vibration and (b) *snap-through* response. (For interpretation of the references to color in this figure legend, the reader is referred to the web version of this article.)

from vibrations around *I* equilibrium (Figs. 15 and 22) the value of the δ parameter is equal 0.7 V. The energy recovery efficiency index calculated from Eq. (15) for both motion variants was 0.0137 mW/V and 0.0152 mW/V for Figs. 22a and 22b, respectively. The η index for *I*-regular vibrations with or without period doubling has similar values. The case with period doubling has a slightly larger value. In two subsequent cases (Figs. 14 and 23) the δ parameter takes value 2 V. For the *snap-through* case, where responses are mix of vibrations around *I* and *C* equilibria. However, the strain average is estimated to be about 2 V. The calculation of the η parameter gave the values 0.026 mW/V and 0.0388 mW/V for *C*-regular vibration and *snap-through* vibration, respectively. These values are two or more times larger than for *I* vibrations cases. Therefore, the proposed η index confirmed that more energy can be recovered from *C*-regular or *snap-through* vibrations. The change of the shape of the vibrating shell to *I* shape affects the efficiency of energy harvesting. As result of experimental data, different values of the so-called electromechanical coupling coefficient should be assumed for the motion around *I* and *C* equilibria in the modeling process.

5. Conclusions and further developments

In this work the nonlinear dynamics and the ensuing vibration energy harvesting performance of a cantilever composite bistable shell were experimentally investigated. The shell manufacturing process was described in detail paying particular attention to the

description of the actual curved geometry and the thickness deviations. Despite imperfections, after clamping the shell exhibited the predicted bistability as well as the sought dynamic reversible *snap-through*. The nonlinear dynamic behavior of the shell was studied through an extensive experimental campaign. The shell dynamic response to harmonic excitation applied at the clamped edge was measured in terms of strain. Starting from each stable equilibrium configurations, namely *I* and *C*, frequency and excitation amplitude sweeps were performed to obtain resonance curves, Poincaré maps and response spectral contents. For low excitation level (amplitude of kinematic excitation lower than 0.6 g) local in-well dynamics around the *I* and *C* stable equilibria is observed. The frequency-response curve related to the *C* stable equilibria turned out to be almost linear, with a slight softening behavior, while the frequency-response curve related to the *I* stable equilibria turned out to be nonlinear with a very strong softening effect and evident asymmetric oscillations. For excitation amplitudes greater than 0.6 g, period doubling and cross-well dynamics involving reversible *snap-through* motion were identified. Overall, the experimental campaign enabled to identify four possible regimes: a periodic in-well vibration around the *C* configuration, a reversible *snap-through* motion, a 1 : 1 and a 2 : 1 periodic in-well vibrations around the *I* configuration. To demonstrate the global picture of the dynamics of the shell, two maps were constructed which allow to identify, for each pair of amplitude and frequency values, the number and type of possible motions. Starting from these maps, the efficiency of the different motions with respect to the energy harvesting capacity was then evaluated. To this aim, a new index based on RMS values of shell strains and harvested electrical power was proposed. The index gave evidence that the periodic in-well vibrations around the *C* configuration and reversible *snap-through* motion provide the highest values of recovered energy. Further developments will address the energy harvesting opportunities offered by cantilever shells characterized by clamped and free edges with opposite curvatures.

Declaration of competing interest

The authors declare the following financial interests/personal relationships which may be considered as potential competing interests: Andrzej Mitura, Lukasz Kloda and Jerzy Warminski report financial support provided by National Science Centre Poland.

Data availability

Data will be made available on request.

Acknowledgments

This research was funded in whole or in part by National Science Centre, Poland 2021/41/B/ST8/03190. For the purpose of Open Access, the author has applied a CC-BY public copyright licence to any Author Accepted Manuscript (AAM) version arising from this submission.

References

- [1] S. Barbarino, O. Bilgen, R.M. Ajaj, M.I. Friswell, D.J. Inman, A review of morphing aircraft, *J. Intell. Mater. Syst. Struct.* 22 (9) (2011) 823–877.
- [2] B.A. Darmawan, D. Gong, H. Park, S. Jeong, G. Go, S. Kim, K.T. Nguyen, S. Zheng, M. Nan, van Nguyen, D. Bang, C. Kim, H. Kim, J. Park, E. Choi, Magnetically controlled reversible shape-morphing microrobots with real-time X-ray imaging for stomach cancer applications, *J. Mater. Chem. B* 10 (23) (2022) 4509–4518.
- [3] Y. Li, Y. Zhao, Y. Chi, Y. Hong, J. Yin, Shape-morphing materials and structures for energy-efficient building envelopes, *Mater. Today Energy* 22 (7) (2021) 100874.
- [4] A. Speciale, R. Arditto, M. Baù, M. Ferrari, V. Ferrari, A.A. Frangi, Snap-through buckling mechanism for frequency-up conversion in piezoelectric energy harvesting, *Appl. Sci.* 10 (10) (2020) 3614.
- [5] Y. Liu, X. Li, M. Yang, J. Zhao, W. Wang, Study on dynamic characteristics of the bistable nonlinear damper, *Appl. Sci.* 13 (2) (2023) 878.
- [6] S.A. Emam, D.J. Inman, A review on bistable composite laminates for morphing and energy harvesting, *Appl. Mech. Rev.* 67 (6) (2015) 175.
- [7] Z. Zhang, Y. Li, X. Yu, X. Li, H. Wu, H. Wu, S. Jiang, G. Chai, Bistable morphing compos. struct.: A review, *Thin-Walled Struct.* 142 (6) (2019) 74–97.
- [8] C.G. Diaconu, P.M. Weaver, A.F. Arrieta, Dynamic analysis of bi-stable composite plates, *J. Sound Vib.* 322 (4–5) (2009) 987–1004.
- [9] A.F. Arrieta, S.A. Neild, D.J. Wagg, Nonlinear dynamic response and modeling of a bi-stable composite plate for applications to adaptive structures, *Nonlinear Dyn.* 58 (1–2) (2009) 259–272.
- [10] A.F. Arrieta, S.A. Neild, D.J. Wagg, On the cross-well dynamics of a bi-stable composite plate, *J. Sound Vib.* 330 (14) (2011) 3424–3441.
- [11] A.F. Arrieta, G. Spelsberg-Korspeter, P. Hagedorn, S.A. Neild, D.J. Wagg, Low order model for the dynamics of bi-stable composite plates, *J. Intell. Mater. Syst. Struct.* 22 (17) (2011) 2025–2043.
- [12] A. Firouzi-Nejad, S. Ziaei-Rad, M. Moore, Vibration analysis of bi-stable composite cross-ply laminates using refined shape functions, *J. Compos. Mater.* 51 (8) (2017) 1135–1148.
- [13] Z. Wu, H. Li, M.I. Friswell, Advanced nonlinear dynamic modelling of bi-stable composite plates, *Compos. Struct.* 201 (6) (2018) 582–596.
- [14] S.A. Emam, Snapthrough and free vibration of bistable composite laminates using a simplified Rayleigh-Ritz model, *Compos. Struct.* 206 (1129) (2018) 403–414.
- [15] W. Zhang, Y.Z. Liu, M.Q. Wu, Theory and experiment of nonlinear vibrations and dynamic snap-through phenomena for bi-stable asymmetric laminated composite square panels under foundation excitation, *Compos. Struct.* 225 (2019) 111140.
- [16] M.Q. Wu, W. Zhang, Y. Niu, Experimental and numerical studies on nonlinear vibrations and dynamic snap-through phenomena of bistable asymmetric composite laminated shallow shell under center foundation excitation, *Eur. J. Mech. - A/Solids* 89 (2021) 104303.
- [17] T. Liu, W. Zhang, Y. Zheng, Y.F. Zhang, W. Zhao, Potential well evolution and metastable dynamics of bistable asymmetric laminated composite square shallow shell under external and parametric excitations, *Compos. Struct.* 280 (2) (2022) 114936.
- [18] M.Q. Wu, W. Zhang, D. Chronopoulos, Nonlinear vibrations and dynamic snap-through behaviors of four-corner simply supported bistable asymmetric laminated composite square shell, *Mech. Syst. Signal Process.* 173 (1) (2022) 109023.

- [19] X.T. Guo, W. Zhang, Y.F. Zhang, Snap-through and nonlinear oscillations of bistable asymmetric FCSS composite laminated square plate subjected to excitation: Theoretical, numerical and experimental researches, *Thin-Walled Struct.* 179 (2022) 109669.
- [20] M. Brunetti, A. Mitura, F. Romeo, J. Warminski, Nonlinear dynamics of bistable composite cantilever shells: An experimental and modelling study, *J. Sound Vib.* 526 (2) (2022) 116779.
- [21] M. Brunetti, A. Vincenti, S. Vidoli, A class of morphing shell structures satisfying clamped boundary conditions, *Int. J. Solids Struct.* 82 (6) (2016) 47–55.
- [22] M. Brunetti, L. Kloda, F. Romeo, J. Warminski, Multistable cantilever shells: Analytical prediction, numerical simulation and experimental validation, *Compos. Sci. Technol.* 165 (14) (2018) 397–410.
- [23] M. Brunetti, S. Vidoli, A. Vincenti, Bistability of orthotropic shells with clamped boundary conditions: An analysis by the polar method, *Compos. Struct.* 194 (9) (2018) 388–397.
- [24] M. Brunetti, A. Favata, S. Vidoli, Enhanced models for the nonlinear bending of planar rods: Localization phenomena and multistability, *Proceed. Math. Phys. Eng. Sci.* 476 (2242) (2020) 20200455.
- [25] L.L. Ren, W. Zhang, Y.F. Zhang, Dynamic snap-through and nonlinear vibrations of bistable asymmetric cross-ply composite laminated cantilever shell under external excitation, *Mech. Syst. Signal Process.* 195 (1) (2023) 110193.
- [26] A.F. Arrieta, P. Hagedorn, A. Erturk, D.J. Inman, A piezoelectric bistable plate for nonlinear broadband energy harvesting, *Appl. Phys. Lett.* 97 (10) (2010) 104102.
- [27] D.N. Betts, C.R. Bowen, H.A. Kim, N. Gathercole, C.T. Clarke, D.J. Inman, Nonlinear dynamics of a bistable piezoelectric-composite energy harvester for broadband application, *Eur. Phys. J. Special Top.* 222 (7) (2013) 1553–1562.
- [28] D.N. Betts, H.A. Kim, C.R. Bowen, D.J. Inman, Optimal configurations of bistable piezo-composites for energy harvesting, *Appl. Phys. Lett.* 100 (11) (2012) 114104.
- [29] David N. Betts, H. Alicia Kim, Christopher R. Bowen, Daniel J. Inman, Optimization of piezoelectric bistable composite plates for broadband vibrational energy harvesting, in: Henry A. Sodano (Ed.), *Active and Passive Smart Structures and Integrated Systems 2012*, in: SPIE Proceedings, SPIE, 2012, p. 83412Q.
- [30] G. Jiang, T. Dong, Z. Guo, Nonlinear dynamics of an unsymmetric cross-ply square composite laminated plate for vibration energy harvesting, *Symmetry* 13 (7) (2021) 1261.
- [31] P. Harris, C. Bowen, D. Betts, A. Kim (Eds.), *Manufacture and characterisation of piezoelectric broadband energy harvesters based on asymmetric bistable laminates*, American Society of Composites Conference, 2014.
- [32] M.S. Taki, R. Tikani, S. Ziaei-Rad, A. Firouzian-Nejad, Dynamic responses of cross-ply bi-stable composite laminates with piezoelectric layers, *Arch. Appl. Mech.* 86 (6) (2016) 1003–1018.
- [33] Andrew J. Lee, Daniel J. Inman, Electromechanical modelling of a bistable plate with macro fiber composites under nonlinear vibrations, *J. Sound Vib.* 446 (6) (2019) 326–342.
- [34] A. Elsheikh, Bistable morphing composites for energy-harvesting applications, *Polymers* 14 (9) (2022).
- [35] J.M. Hodgkinson, *Mechanical Testing of Advanced Fibre Composites*, CRC Press and Woodhead, Boca Raton [etc.] and Cambridge, 2000.
- [36] **Smart-Material**, (2023) URL <https://www.smart-material.com/>.
- [37] J. Warminski, A. Mitura, K. Jankowski, Regular and chaotic vibrations of a preloaded pendulum system, *J. Theor. Appl. Mech.* (46) (2008) 223–234.